Journal of Materials Chemistry A

Accepted Manuscript

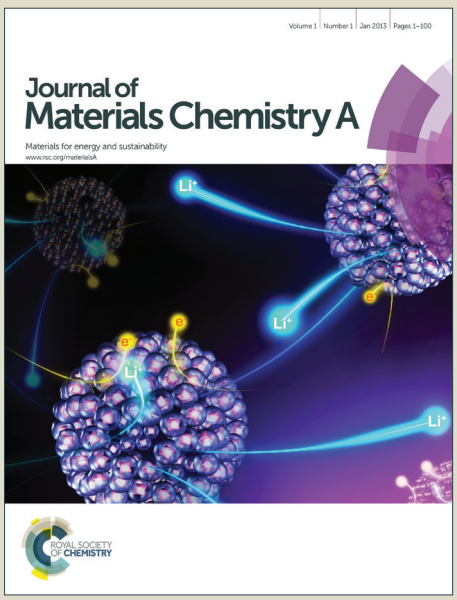

ROYAL SOCIETY OF CHEMISTRY

www.rsc.org/materialsA

Facile hydrothermal synthesis of crystalline Ta_2O_5 nanorods, $MTaO_3$ (M=H, Na, K, Rb) nanoparticles, and their photocatalytic behaviour.

Dorothea Gömpel, Muhammad Nawaz Tahir, Martin Panthöfer, Enrico Mugnaioli, Robert Brandscheid, Ute Kolb, Wolfgang Tremel*

Received (in XXX, XXX) Xth XXXXXXXXX 200X, Accepted Xth XXXXXXXXX 20XX
First published on the web Xth XXXXXXXXX 20XX
DOI: 10.1039/b000000x

Alkali metal tantalates are of interest for applications in photocatalysis as well as in high temperature resistance or capacitor dielectric materials. We have synthesized nanosized Ta_2O_5 rods and $MTaO_3$ cubes (M=Na, K, Rb) hydrothermally and demonstrate the pH dependence of the synthesis of tantalum oxide and tantalate nanoparticles. The morphologies of the nanoparticles range from particle agglomerates in acidic reaction media over rods at neutral pH to tantalate cubes in basic reaction media. Whereas there is no apparent influence of the base cation on the particle morphology, there is a pronounced effect on the particle composition. At high base concentrations cubic tantalate particles with a pyrochlore structure were formed. The pyrochlor structure allows a complete ion exchange through the tunnels in the structure by replacing the alkali metal ions by H^+ while retaining the particle morphology. The as-synthesized particles show promising photocatalytic properties.

Introduction

One of the challenging issues in nanotechnology is the ability to establish protocols for the scalable synthesis, and enhanced properties of nanoscale engineered advanced materials. Many improved pathways for the synthesis of such nanomaterials with tunable properties have been recently reported.[1] Among transition metal oxides, tantalum pentoxide (Ta_2O_5) has proven as a potential candidate in electronics and photoelectrics due to its high dielectric constant, high refractive index, low internal stress and high resistivity.[2-4] Ta_2O_5 has also been used as anti-reflection layer in solar cells and nonlinear optical applications.[5] Moreover, it shows very good thermochromic properties, and its optical properties can be altered by raising the temperature. Furthermore such systems can be employed in solid electrolyte fuel cells and waste water recovery.[6,7] However, unlike for other metal oxides, reports on a controlled synthesis of tantalum oxide in the nanoregime are scarce. Hydrothermal,[8-15] solvothermal,[16-19] sol-gel approaches,[20,21] ultrasonic methods,[22] reactions in microemulsions,[23-26] and templating methods[27-30] have been applied to synthesize Ta_2O_5 and alkali metal tantalate ($NaTaO_3$ and $KTaO_3$) nanoparticles and powders.[31-38] The majority of the reported $NaTaO_3$ and $KTaO_3$ particles exceed the size of 100 nm, and the major drawback of most these methods reported for the synthesis of Ta_2O_5 nanoparticles is the lack of crystallinity. Therefore, these nanoparticles always require a thermal post treatment above 600 °C[16] to improve crystallization. Only recently Ta_2O_5 nanorods[9] and flowerlike Ta_2O_5 nanostructures[29] were obtained by a hydrothermal method using hydrofluoric acid. Synthetic routes avoiding the use of toxic chemicals are highly desirable.

In this article, we describe a versatile hydrothermal method which allows to obtain crystalline Ta_2O_5 nanorods without further heat treatment. In addition, various cubic alkali metal (Na, K, Rb) tantalate nanoparticles were obtained, of which especially $Rb_2Ta_2O_6$ has not been reported before. Additionally, cubic Ta_2O_5 nanoparticles were synthesized via fast ion exchange of the tantalates and subsequent heat treatment. Moreover, we present a systematic study to evaluate the influence of the reaction pH value as well as the respective precursor base for the composition and morphology of the nanoparticles. The reactivity of the tantalates in terms of ion exchange was monitored, and the photocatalytic activity of the prepared materials was studied by monitoring the degradation of rhodamine B as a model substrate.

Experimental section

Materials

All chemicals were used without further purification. Tantalum(V) ethoxide (99.98%), sodium hydroxide (pellets, p.a.), potassium hydroxide (flakes, p.a.), and rubidium hydroxide hydrate were purchased from Sigma Adrich. Tantalum(V) *n*-butoxide (95%) and rubidium hydroxide solution (50 wt%,99%) were obtained from ABCR, ethanol (p.a.) from VWR, and a 0.1 N sodium hydroxide stock solution from Roth.

Synthesis

Synthesis of alkali tantalates with cubic morphology. In a typical reaction 0.335 mL (0.80 mmol) of tantalum(V) *n*-butoxide was added in a beaker to 4 mL of ethanol. The sol was aged in a desiccator under humid atmosphere by keeping a petri dish containing water at the bottom of desiccator over a period of 20 h. The formed gel was mixed with 20 mL of a solution containing 0.1 M of the respective alkali hydroxide (potassium hydroxide, rubidium hydroxide or sodium hydroxide solution, respectively). The resulting solutions were transferred into a 50 mL teflon lined autoclave and kept at 200 °C for 60 h. Finally, the contents of the reaction vessels were cooled to room temperature, the product was separated by centrifugation using 9000 rpm for 15 min. The

obtained product was further purified by washing twice with 20 mL water each time.

Synthesis of $HTaO_3$ by ion exchange of the alkali tantalate nanoparticles. The as-prepared samples were sonicated with 20 mL of (2M) hydrochloric acid for 30 min, centrifuged, washed with 25 mL water followed by 25 mL ethanol. The particles were dried in vacuo overnight.

Annealing of the $HTaO_3$ nanoparticles. $HTaO_3$ nanocubes were heated to 750 °C over 3 h and maintained at that temperature for 12 h.

Synthesis of the Ta_2O_5 nanorods. Ta_2O_5 nanorods were synthesized by gelation of tantalum(V) *n*-butoxide, carried out as described above for the synthesis of cube-shaped alkali tantalates. The formed gel was transferred in a 50 mL Teflon lined autoclave together with 20 mL of a 5 mmol base solution, sealed, and kept at 200 °C for 60 h. The resulting colorless solid was centrifuged (15 min, 9000 rpm) and washed twice with 20 mL water.

Annealing of the Ta_2O_5 nanorods. The as-synthesized nanorods were dried using a vacuum line overnight, and subsequently heated to 850 °C in a corundum boat with heating rate 5 °C per min for 12h.

Materials Characterization

TEM, HRTEM, EDX. The nanoparticles were characterized by transmission electron microscopy (TEM) using a Philips EM420 instrument with an acceleration voltage of 120 kV. TEM samples were prepared by dropping a dilute ethanolic suspension of the nanoparticles on a carbon coated copper grid. High resolution (HR) TEM images, and energy dispersive X-ray (EDX) spectroscopy were acquired on a FEI Tecnai F30 S-Twin microscope with a 300 kV field emission gun. TEM/HRTEM images and FFT patterns were acquired with a CCD camera (14-bit GATAN 794MSC). For a quantitative EDX analysis carbon coated gold or nickel grids were used to avoid the overlap of the Ta L-lines (11.67-7.173 keV) with the Cu K-lines (8.048-8.028 keV). EDX spectra were acquired and quantified with the Emispec ESVision software.

X-ray techniques. Powder X-ray diffraction patterns were recorded with a Siemens D5000 diffractometer equipped with a Braun M50 position sensitive detector in transmission mode using Ge (200) monochromatized CuK_α radiation. Samples were prepared between two layers of Scotch Magic. Phase analyses were performed according to the PDF-2 using Bruker AXS EVA 10.0

Rietveld refinements for quantitative phase analysis, determination of the composition and evaluation of crystallite sizes, respectively, were performed according to reported structure models using Topas Academic V4.1.[39] Reflection profiles were generated according to the fundamental parameter approach[40] applying a correction for anisotropic crystallite morphologies. Within this model individual crystallite ($CS_{\underline{h}}$) sizes are computed for each reflection (*hkl*) according to the quadratic form $CS_{\underline{h}} = {}^{1}/_{\text{norm}} \{ \underline{h}^{T} \times \underline{\underline{C}}_{ij} \times \underline{h} \}$ in which $\underline{h}$ is the reciprocal lattice vector corresponding to (*hkl*) and $C_{ij} = (a_i)^{½} \times (a_j)^{½}$ is the symmetric second rank tensor of the square roots of the crystallite dimensions in direction *i* and *j* in the basis of the crystal lattice.

X-ray fluorescence (XRF) measurements were carried out on a PANalytical aXios 4 kW instrument using SuperQ/OMNIAN V 5.0D PANalytical B.V., Almelo, Netherlands (2009). The samples (20 mg) were measured in a boronic acid pellet (2 g) as matrix.

Photocatalytic measurements. Freshly prepared solutions (0.5 mg/mL) of as synthesized nanoparticles mixed with rhodamine B (RhB) solution (0.001 mg/mL) were irradiated under a 8 W UV-Lamp using UV-light having wavelength (λ)= 254nm and 366 nm. UV-VIS spectra were measured using a Cary Varian 5G UV-VIS-NIR spectrometer.

Results and Discussion

3.1. Influence of the pH value

In order to demonstrate the effect of pH on the morphology, various experiments were performed by changing the amount of added base (NaOH) while keeping all other papermeters constant.

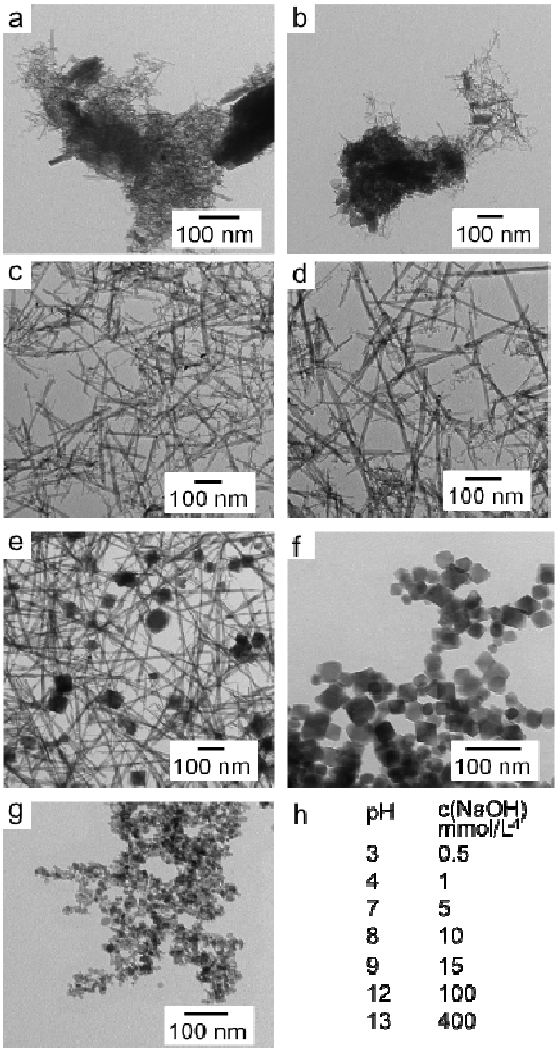

Fig. 1.a-g) TEM micrographs of the tantalum oxide nanoparticles at different pH values. a) pH=3, b) pH=4, c) pH=7, d) pH=8, e) pH=9, f) pH=12 and g) pH=13. h) shows the pH values of the reaction mixtures before the hydrothermal treatment based on NaOH concentration.

The products were characterized using TEM. TEM and representative overview TEM images shown in Fig. 1 show the particle morphologies obtained at different pH values. For pH=3

and pH=4 only one crystalline phase was found. However there might be amorphous phases that are unaccounted for. At pH=3 (Fig. 1a) and pH=4 (Fig. 1b) a mixture of small needles along with big agglomerates were obtained. A snapshot after 12 h was taken which also yielded agglomerates (see SI Fig. S1). At pH=7 (Fig. 1c) and pH=8 (Fig. 1d) rod-shaped nanoparticles with a broad distribution of size and aspect ratio were formed.The average width of the rods is about 9 nm for pH=7 and pH=8 whereas the length of the rods vary between 30 nm and 600 nm. In contrast to an acidic reaction medium there is no agglomeration of the nanorods at near neutral pH values. Fig. 1f and g show the cube-shaped morphology of the nanoparticles obtained at pH=12 and pH=13. The distorted cuboidal nanoparticles at pH=13 exhibit a higher polydispersity than the ones obtained at pH=12. Additionally the particles are smaller and have a mean length of 12±6nm (histogram see Fig. S2). In Fig. 1e (corresponding to a pH value of 9) nanorods and parallelepiped-shaped nanoparticles coexist. Fig 1h compiles the NaOH concentrations used to obtain the different pH values in the reaction mixture before hydrothermal treatment. There is no change of the pH values during the reaction as confirmed by pH measurements after the reaction. According to the x-ray diffraction investigations the crystalline products formed upon reaction at pH = 3 and pH = 4 are single phase Ta_2O_5. The (*00l*) reflections exhibit significantly sharper reflection profiles than reflections of general (*hkl*). This points to anisotropic crystallite sizes and was therefore taken into account in the corresponding refinements. The crystallite sizes determined this in this way are 41(1) nm in the *a,b* plane and 70(1) nm in *c* direction for the nanorods obtained at pH = 3 and 47(1) nm in *a,b* plane vs. 75(1) nm in *c* direction for the nanorods obtained from the reaction carried out at pH = 4.

The x-ray diffraction patterns of the products prepared at pH-values of 7 and 8 exhibit still the reflections corresponding to Ta_2O_5. Yet, the profiles of the Ta_2O_5 phase are broader and additional, very broad intensities of a non-identified phase appeared.

X-ray diffraction patterns of the products prepared at pH values of 9, 12 and 13 exhibit the reflections of defect-pyrochlore-type tantalic acid "$HTaO_3$".[41] The product prepared at pH = 9 is a mixture of tantalic acid with Ta_2O_5 (15(1) %wt, crystallite size 48(2)) whereas the one prepared at pH = 13 is a mixture of tantalic acid with $NaTaO_3$[41] (17(2) %wt, crystallite size > 100nm). The product prepared at pH = 12 is single phase pyrochlore-type tantalic acid and exhibits the highest crystallinity within the series of different pH values, i.e. 47(1) nm at pH = 12 vs. 33(1) nm at pH = 9 and 21(1) nm at pH = 13. The crystal chemistry and in particular the exact structure and composition of the defect-pyrochlore-type group V and VI metal acids is a complex matter that cannot be resolved from laboratory x-ray diffraction data of nanoparticular samples. On the other hand, the Rietveld refinements for the pH = 9, pH = 12 and pH = 13 samples point to substantial amounts of sodium cations on the proton positions. The refinements were therefore performed assuming an idealized composition $H_{2-x}Na_{2x}Ta_2O_6{\cdot}yH_2O$ with protons and sodium cations on the 16*d* site and water molecules of crystallization on the 8*b* site. At pH = 9 virtually all protons are substituted (x = 2.00(6)), increasing the pH value their amount decreases to x = 0.84(1) at pH = 12 and x = 0.78(2) at pH = 13, which are identical within 1σ. For further details see Tab. S1.

For large-scale synthesis reactions can be carried out in an 250 mL autoclave yielding up to 800 mg in one batch (see SI Fig. S1). In summary, there is a strong dependence of the morphology as well as the composition of the tantalum oxide species on the pH value. This influence can partially be understood as analogous to the Stöber process with silica.[42] The occurrence of agglomerates at low pH values can be assigned to a fast hydrolysis rate at low pH values compared to higher ones. Additionally the acidic surface of tantalum oxide facilitates the agglomeration of nanoparticles.

With increasing pH the sodium concentration rises and the formation of sodium tantalate occured rather than that of tantalum oxide. The cubic unit cell of the nanoparticles is responsible for the cube -like morphology of the product instead of rods obtained at lower pH. Hence the pH value is a valuable tool for tuning the morphology of the product.

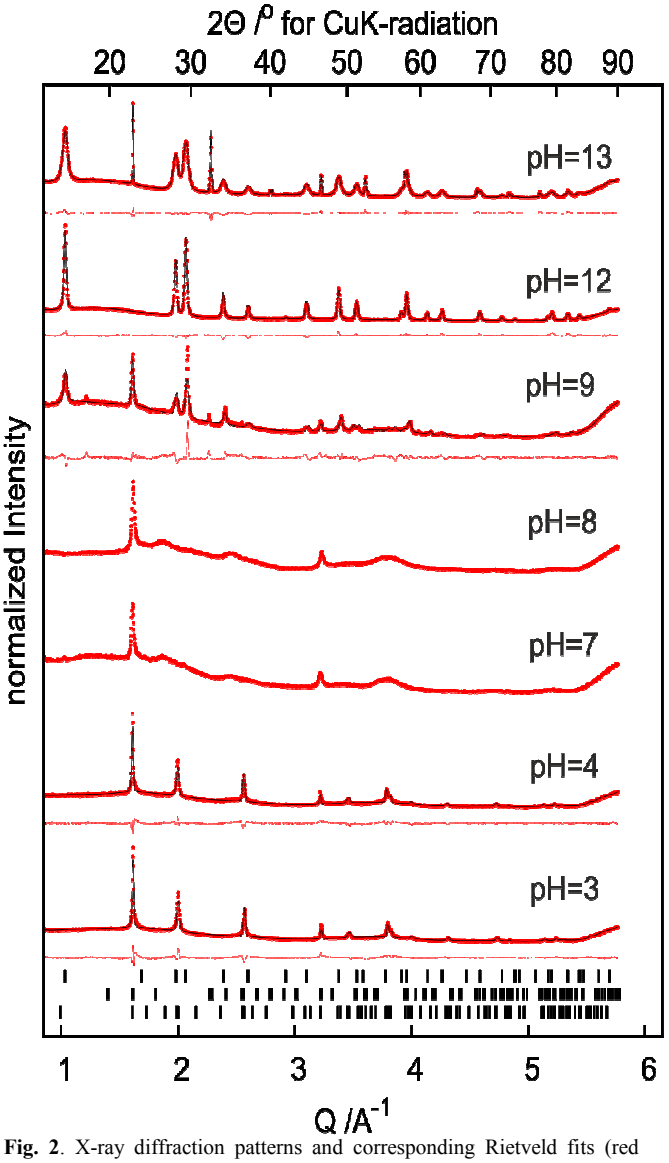

Fig. 2. X-ray diffraction patterns and corresponding Rietveld fits (red dots: observed intensity, black line: fit, red line: difference curve) of the products prepared at different pH values and corresponding tic marks of $HTaO_3$ (top), $NaTaO_3$ (middle) and Ta_2O_5 (bottom).

After submission of this paper Kanhere et al.[15] reported that at a higher NaOH concentration favors the formation of perovskite $NaTaO_3$ over the pyrochlore $Na_2Ta_2O_6$. The work reported here is not only restricted to NaOH as a base; we have used different bases and additionally show the importance of different counter ions (K, Rb) on the particle morphology. Furthermore the examined base concentrations in our and Kanhere´s work differ. Kanhere concentrates on high base concentrations yielding only cubic particles while we worked with lower concentrations. Therefore we were able to see a significant change in morphology from anisotropic rods to more symmetric cube-shaped particles.

3.2. Influence of the base (counter cation) at pH=7 and pH=12

As we observed that neutral or basic pH values of 7 and 12 resulted in the formation of well-defined nanorods and cube-shaped nanoparticles, we decided to use these conditions to explore the effect of the counter cation while maintaining the other parameters constant. In order to evaluate the influence of the cation, NaOH, KOH and RbOH were used as precursor bases with concentrations of 5 mM and 100 mM, respectively. The pH value before and after the reaction was neutral for all used bases with a base concentration of 5 mM. When a 100 mM base solution was used the pH was 12 for all precursor bases, before and after the reaction.

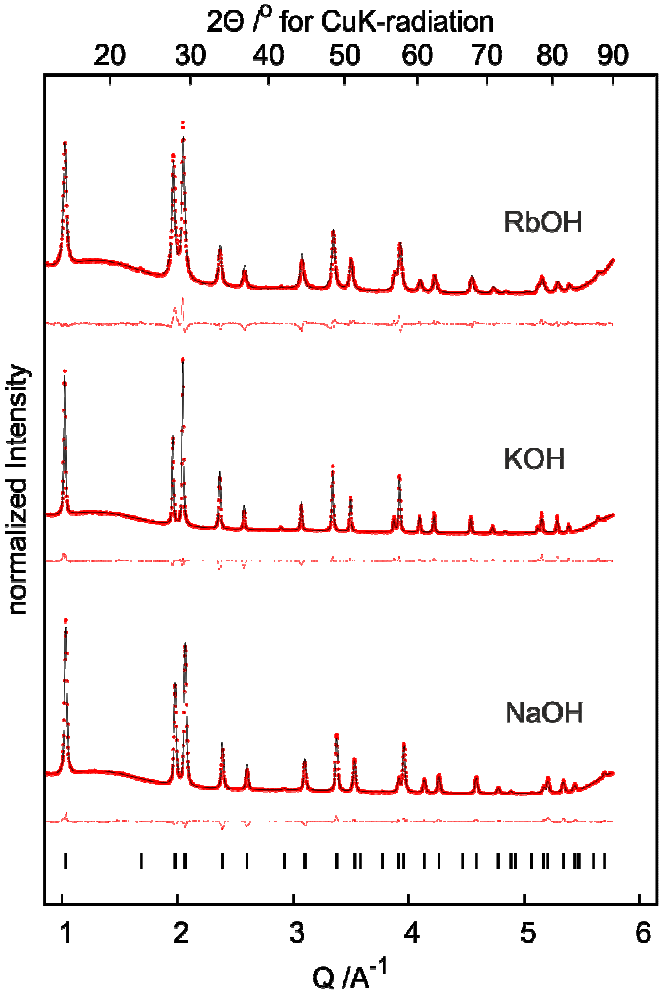

Fig. 3. X-ray diffraction patterns and corresponding Rietveld fits (red dots: observed intensity, black line: fit, red line: difference curve) of the products prepared with 0.1 m RbOH, KOH or NaOH respectively. Bottom tic marks for the pyrochlor structure.

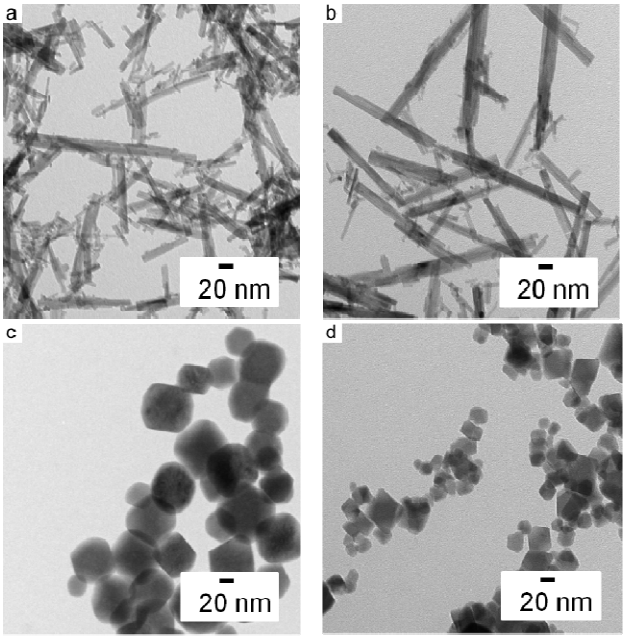

Fig. 4. TEM images of the nanoparticles yielded with different bases at different pH values. a) pH=7 with KOH, b) pH=7 with RbOH as precursor base and c) KOH and d) RbOH as precursor base both at pH=12.

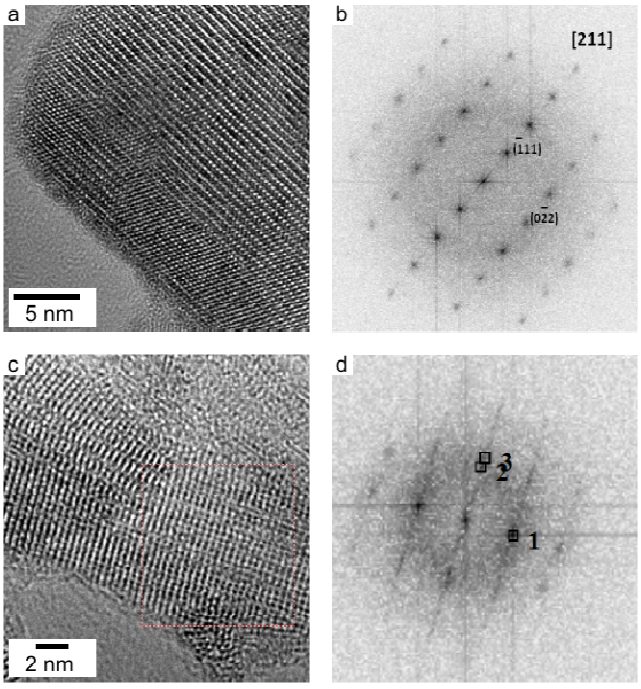

Fig. 5. a) HR-TEM picture of the cubes with 0.1 M RbOH and corresponding b) fast fourier transform (FFT). The inset shows the corresponding electron diffraction pattern. c) HR-TEM picture of the Ta_2O_5 nanorods synthesized with 5 mM RbOH. d) FFT of the nanorods shown in c).

In order to clarify the phase composition of the as synthesized products with 100 mM NaOH, KOH and RbOH x-ray powder diffraction data were collected. The x-ray diffraction patterns shown in Fig. 3 resemble that of the defect-pyrochlore tantalic acid. According to the Rietveld refinements (cf. Tab. S2), the approximate composition of the samples is $Na_{0.88}H_{1.12}Ta_2O_6 \times 0.37$

H_2O, $K_{0.97}H_{1.03}Ta_2O_6$ and $Rb_{0.2}H_{1.8}Ta_2O_6{\times}H_2O$. XRF measurements were carried out to determine the ratio between the tantalates and tantalic acid in the nanoparticles (Tab. S3). For RbOH an atomic ratio of Rb:Ta of 1:1.27 was found.

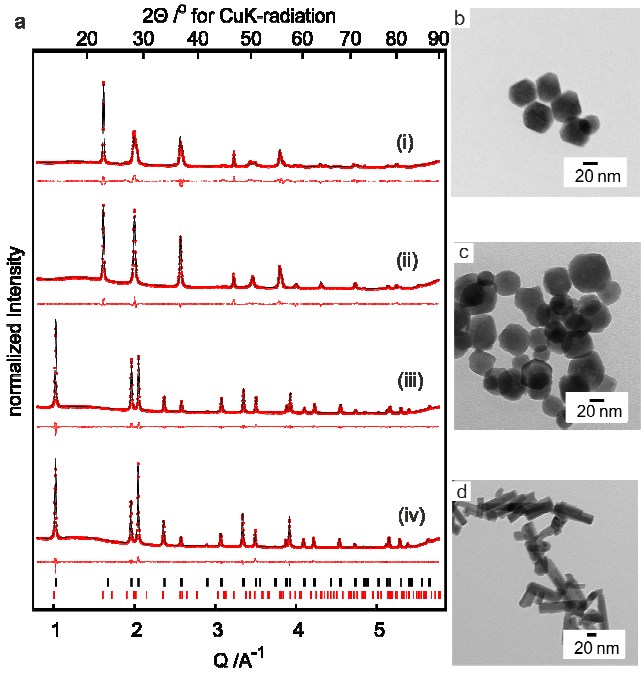

Fig. 3. a) X-ray diffraction patterns and corresponding Rietveld fits (red dots: observed intensity, black line: fit, red line: difference curve) of (i) tantalum oxide rods after annealing at 850 °C for 12 h (ii) cubes after annealing at 750 °C for 12 h (iii) tantalates after and (iv) before acid treatment. TEM image of b) the tantalate nanoparticles after acid treatment. c) Heat treated cubes after 12 h at 750 °C and d) heat treated nanorods after 12 h at 850 °C.

When KOH was used as a base to keep the pH constant, an K:Ta atomic ratio of 1:2.19 was obtained (see Tab. S3, supporting information). The discrepancy between the compositions determined from the XRD and the XRF data indicates the principal limits of x-ray diffraction for the analysis of nanomaterials. TEM images (Fig. 4) show the morphologies of the nanoparticles synthesized at pH 7 with 5 mM KOH (a) and RbOH (b). A TEM micrograph with the same magnification for 5 nM NaOH can be found in the supporting information Fig. S3. In each case (e.g. for NaOH in Fig. 1c) non-agglomerated nanorods were obtained. The product exclusively contained anisotropic particles. The mean width of the nanorods is 8 nm for both RbOH and KOH. Fig. 4c and d show TEM images of nanoparticles obtained from solutions containing 100 mM of KOH and RbOH. With KOH, cubic nanoparticles with almost round edges were obtained having an average length of 34±7 nm. No differences in morphology were found between products with either KOH or NaOH. However, when RbOH was used to adjust the pH, cube-shaped nanoparticles with a slightly broader size distribution of 26±13 nm were obtained (compared to nanoparticles obtained using KOH)(see Fig. S4). The HRTEM images in Fig. 5 reveal details of the crystal structure of the cubes as well as the rods. The HRTEM image of the nanoparticles from 100 mM RbOH solution (Fig. 5a) indicates that the particles are mesocrystalline, i.e. they consist of individual small crystallites. The crystallinity of the nanocubes was confirmed by nano-electron diffraction (NED, Fig. 5b). A HRTEM image of the nanorods (Fig. 5c) reveals stacking and lateral disorder in the rods. The fast Fourier transform (FFT) image (Fig. 5d) corroborates the model of crystallinity even though the reflections are blurred due to disorder in the observed area. EDX was performed on the rods to confirm the elemental composition which shows only (Fig. S5) the presence of tantalum and oxygen without having any trace amounts of rubidium. This is due to the low alkali metal concentration in the solutions. The powder X-ray patterns of products obtained with 5mM NaOH, KOH and RbOH are shown in Fig. S6.

3.3 Ion exchange in the tantalates and heat treatment

Ion exchange in the pyrochlore structures is a known phenomenon where the alkali metal ions on the intrachannel positions of the pyrochlore framework can be replaced by other cations like H_3O^+ [40] or Pb^{2+}.[6] This offers the opportunity to change the composition of the nanoparticles from tantalates to tantalic acid without a change in morphology. Hence the tantalates were treated with dilute HCl to replace M^+ (M=Na, K, Rb) in the structure by H_3O^+. For ion exchange experiments the tantalate nanoperticles synthesized with 100 mM KOH, NaOH and RbOH, respectively, were used. TEM measurements of the HCl treated tantalate nanoparticles (Fig. 6b) revealed no apparent change in morphology or size distribution during the treatment with HCl the nanoparticles maintain their cubic shape and remain faceted. The extent of the ion exchange was monitored by XRF. The K:Ta ratio of the nanoparticles, synthesized with 100 mM KOH, dropped to K:Ta 1:30 after acid treatment. The x-ray diffraction pattern of the ion exchanged sample exhibits significant changes of the intensity of some reflections, i.e. (311), (222), (044) and (622), and a slight shift of all reflection towards higher scattering angles corresponding to a decrease of the lattice parameter from 10.6324(2) Å to 10.6014(2) Å (see Tab. S4). According to the results of the Rietveld refinements the composition changes from $K_{0.97}H_{1.03}Ta_2O_6$ to $H_2Ta_2O_6{\times}0.45H_2O$. Thus, the K^+–ions are fully replaced by protons and additional water molecules of crystalization. The same effect was found for $NaTaO_3$ and $RbTaO_3$, where virtually no traces of alkali metal were found. This corroborates an ion exchange in the tantalate nanoparticles.

Ion exchange opens a route to cube-shaped tantalum oxide nanoparticles via thermal dehydration of $HTaO_3$. TEM images of a samples heated to 750 °C for 12 h confirm that the nanoparticles retain their morphology (Fig. 6c) after heat treatment. The tantalum oxide nanorods were annealed for 12 h at 850 °C to improve their crystallinity. TEM data (Fig. 6d) reavealed the calcinated product to retain a rodlike morphology although the aspect ratio decreased in comparison to the as-synthesized samples. TEM studies showed that the length of the rods decreased while the width increased.

Quantitative phase analyses reveal both heat treated samples to be phase pure orthorhombic Ta_2O_5 (Ta_2O_5-*oP*14). The crystallite sizes of the cubic nanoparticles correspond to an aspect ratio of 1.5, while 2.9 is found for the rods in agreement with the higher anisotropy of the rods compared to the cubes, even at elevated temperatures. Without prior acid treatment of the cubes, no phase transformation occurred up to 750 °C.

The HR-TEM images of the annealed samples (Fig. 7) revealed the detailed crystal structure through their corresponding FFT patterns. For the annealed rods the predominant growth direction is along the [010] direction. The annealed rods (Fig. 7a) show a high degree of disorder orthogonal to the growth direction illustrated by the drawn-out spots in the FFT (Fig. 7b). Disorder is less pronounced in the heat treated cubes (Fig. 7c). However, they are not single crystalline but consist of various crystallites. The FFT analysis shows in agreement with the PXRD data both samples to consist of orthorhombic Ta_2O_5 (Fig. 7c,d).

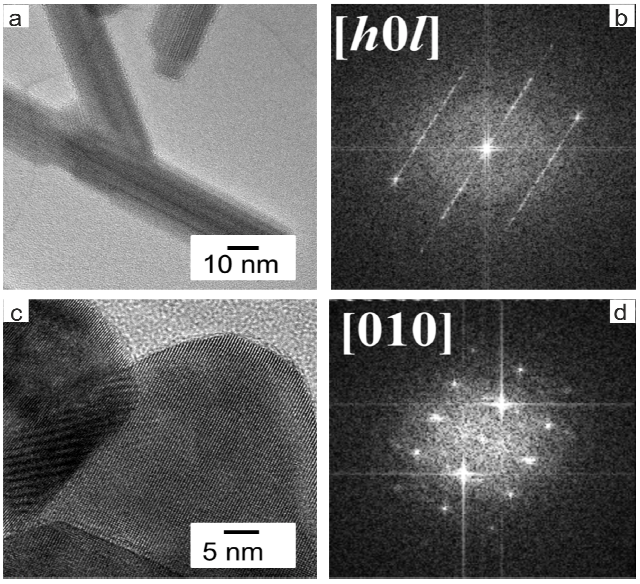

Fig. 4. a) HR-TEM image of the heat treated rods (12h, 850 °C) with b) corresponding FFT pattern and c) HR-TEM image of the heat treated cubes (12h, 750 °C) and its corresponding FFT pattern (d).

3.4. Photocatalytic activity

The photocatalytic activity of the nanoparticles was explored by mixing dispersions with a RhB solution and irradiation with UV light. Fig. 8a shows the UV-VIS spectra of the solutions after centrifuging the nanoparticles exposed to UV-light for 18 minutes. Fig. 8b shows a photograph of the corresponding vials. Cube-shaped $KTaO_3$, $HTaO_3$ and as-synthesized Ta_2O_5 nanorods lead to a complete degradation of RhB dye; no absorbance of RhB could be observed. Virtually no RhB absorbance was found after 8 minutes irradiation for the rods, after 4 minutes for cube-shaped $HTaO_3$ and after 12 minutes for cube-shaped $KTaO_3$. The activity difference between cube-shaped $HTaO_3$ and $KTaO_3$ can be attributed to the acidic groups on the surface of $HTaO_3$, which facilitate the degredation of the dye. An absorbance of RhB can be observed for the both heat treated samples. The absorbance dropped to 22% and 34% compared to the RhB control for the Ta_2O_5 cubes and rods, respectively. As control experiment the samples were stirred with RhB in the dark for 18 min. There was virtually no dye degradation in the dark for all samples as can be seen in the SI (Fig. S7). Possible reasons, why the heat-treated Ta_2O_5 particles did not degrade RhB as fast as the as-synthesized counterpart (in spite of their higher high crystallinity) might be that the crystalline phases for the as-synthesized and heat-treated samples are different or differeces in their surface wettability.

Conclusions

In summary, we synthesized nanosized Ta_2O_5 rods and $MTaO_3$ cubes (M=Na, K, Rb) by a facile hydrothermal route. Furthermore we demonstrated the pH dependence in the synthesis of tantalum oxide and tantalate nanoparticles. Similarly as for titanates,[43] the obtained morphologies range from particle agglomerates in acidic reaction media over rods at neutral pH to tantalate cubes in basic reaction media. Whereas there is no apparent influence of the base cation on the particle morphology,[44] there is a pronounced influence on the particle composition. At high base concentrations cubic tantalate particles with a pyrochlore structure are formed. The pyrochlore structure allows a complete ion exchange through the tunnels in the structure replacing all alkali metal ions with H^+ while retaining the morphology. In addition the as synthesized particles show promising photocatalytic properties.

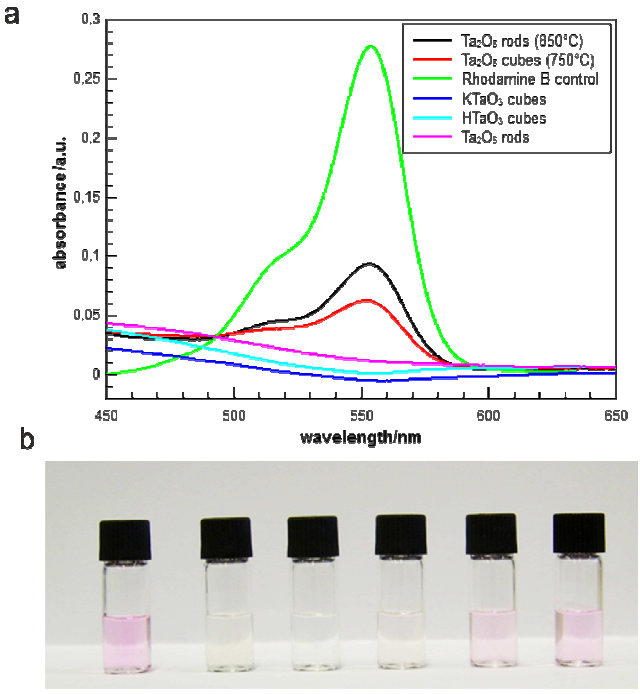

Fig. 5. a) UV-VIS spectra of the samples after UV-light irradiation for 18 minutes and centrifugation of the nanoparticles. b) Digital photograph of the corresponding solutions from left to right: control RhB solution, $KTaO_3$, $HTaO_3$, (cube shape), Ta_2O_5 (rods shape), Ta_2O_5 (cube shape) (750 °C), and Ta_2O_5 (rods shape) (850 °C)

Acknowledgements

We are grateful to the Deutsche Forschungsgemeinschaft (DFG) for support within the priority program 1415 "Kristalline Nichtgleichgewichtsphasen".

Notes and references

[a] *Institut für Anorganische Chemie und Analytische Chemie, Johannes Gutenberg-Universität, Duesbergweg 10-14, D-55099 Mainz, Germany. Fax: +49 6131 39-25605; Tel: +49 6131 39-25135; E-mail: tremel@uni-mainz.de*

[b] *Institut für Physikalische Chemie, Johannes Gutenberg-Universität, Welderweg 11,55099 Mainz, Germany.*

† Electronic Supplementary Information (ESI) available: Photograph of product of an upscaled reaction and TEM image of product at pH = 4 after 12 h (Fig. S1), histograms of $NaTaO_3$ cubes obtained at pH = 12 and pH = 13 (Fig. S2), TEM micrograph of Ta_2O_5 nanorods with 5 mM NaOH (Fig. S3), histograms of $KTaO_3$ and $RbTaO_3$ cubes obtained at pH =12 (Fig. S4), EDX of nanorods obtained with RbOH (Fig. S5), PXRD of the nanorods with NaOH, KOH and RbOH (Fig. S6), and UV-VIS spectra of RhB degradation in the dark (Fig. S7), PXRD measurement and refinement parameters of the products obtained at different pH values (Tab. S1), of the cube-shaped nanoparticles obtained with diferent bases (Tab. S2), X-ray diffraction patterns of the products obtained with NaOH, KOH and RbOH, respectively (Tab. S3), PXRD measurement and refinement parameters of the ion-exchanged and heat treated products (Tab. S4). See DOI: 10.1039/b000000x/

1 C. D. Valenzuela, G. A. Carriedo, M. L. Valenzuela, L. Zuniga and C. O'Dwyer, *Sci. Rep*. 2013, **3**, 2642.
2 D. L. Guyton and F. T. Hambrecht, *Science* 1973, **181**, 74.
3 Y. L. Chueh, L. J. Chou and Z. L. Wang, *Angew. Chem. Int. Ed*. 2006, **45**, 7773
4 L. L. Xu, J. G. Guan, L. Gao and Z. G. Sun, *Catal. Commun*. 2011, **12**, 548.
5 D. Bouhafs, A. Moussi, A. Chikouche and J. M. Ruiz, *Solar Energy Materials and Solar Cells* 1998, **52**, 79.
6 S. N. Britvin, O. I. Siidra, A. Lotnyk and S. V. Krivovichev, *Eur. J. Inorg. Chem*. 2010, 1082
7 F. Baucke, S. Dorner, V. Heinzel and G. Röth, *Materials Science Forum* 1991, **76**, 287
8 J. Shi, G. Liu, N. Wang and C. Li, *J. Mater. Chem.* 2012, **22**, 18808
9 X. Lu, S. Ding, T. Lin, X. Mou and Z. Hong, *Dalton Trans.* 2012, **41**. 622.
10 J. Duan, W. Shi, L. Xu, G. Mou, Q. Xin and J. Guan, *J. Chem. Commun.* 2012, **48**, 7301.
11 Y. Su, S. Wang, Y. Meng, H. Han and X. Wang, *RSC Advances* 2012, **2**, 12932.
12 T. Hashizume, A. Saiki and K. Terayama, *Mater. Trans*. 2010, **51**, 261.
13 L. Huang, Q. Chan, B. Zhang, X. Wu, P. Gao, Z. Jiao and Y. Liu, *Chin. J. Catal.* 2011, *32*, 1822
14 R. Gao, S. Zhou, W. Li, M. Chen and L. Wu, *CrystEngComm* 2012, **14**, 7031.
15 P. Kanhere, Y. Tang, J. Zheng and Z. Chen, *J. Phys. Chem. Solids* 2013, **74**, 1708
16 J. Buha, D. Arcon, M. Niederberger and I. Djerdj, *Phys. Chem. Chem. Phys*. 2010, **12**, 15537.
17 G. Garnweitner and M. Niederberger, *J. Am. Ceram. Soc.* 2006, **89**, 1801.
18 J. Wang, S. Su, B. Liu, M. Cao and C. Hu, *Chem. Commun*. 2013, **49**, 7830.
19 Y. He and Y. Zhu, *Chem. Lett.* 2004, **33**, 900.
20 H. Konminami, M. Miyakawa, S. Murakami, T. Yasuda, M. Kohno, S. Onoue, Y. Kera and B. Ohtani, *Phys. Chem. Chem. Phys.* 2001, **3**, 2697.
21 B. Baruwati and R. Varma, *Cryst. Growth Des.* 2010, **10**, 3424.
22 O. Vázquez-Cuchillo, A. Manzo-Robledo, R. Zanella, N. Elizondo-Villareal and A. Cruz-López, *Ultrason. Sonochem.* 2013, **20**, 498.
23 M. H. Oh, N. Lee, H. Kim, S. P. Park, Y. Piao, J. Lee, S. W. Jun, W. K. Moon, S. H. Choi and T. Hyeon, *J. Am. Chem. Soc.* 2011, **133**, 5508.
24 V. Shanker, S. L. Samal, G. K. Pradhan, C. Narayana and A. K. Ganguli, *Solid State Sci.* 2009, 562.
25 P. J. Bonitatibus, Jr., A. S. Torres, G. D. Goddard, P. F. Fitzgerald and A. M. Kulkarni, *Chem. Commun.,* 2010, **46**, 8956.
26 M. H. Oh, N. Lee, H. Kim, S. P. Park, Y. Piao, J. Lee, S. W. Jun, W. K. Moon, S. H. Choi, T. Hyeon, *J. Am. Chem. Soc.* 2011, **133**, 5508.
27 T. Yokoi, J. Sakuma, K. Maeda, K. Domen, T. Tatsumi and J. Kondo *Phys. Chem. Chem. Phys*. 2011, **13**, 2563-2570
28 S. Lin, L. Shi, H. Yoshida, M. Li and X. Zou *J. Solid State Chem.*, 2013, **199**, 15.
29 J. Duan, W. Shi, L. Xu, G. Mou, Q. Xin and J. Guan, *Chem. Commun*. 2012, **48**, 7301.
30 T. Yokoi, J. Sakuma, K. Maeda, K. Domen, T. Tatsumi, and J. N. Kondo, *Phys. Chem. Chem. Phys*. 2011, **13**, 2563.
31 H. Kato and A. Kudo, *J. Phys. Chem. B* 2001, **105**, 4285.
32 H. Kato and A. Kudo, *Chem. Phys. Lett*. 1998, **295**, 487.
33 C.-C. Hu, C.-C. Tsai and H. Teng, *J. Am. Ceram. Soc*. 2009, **92**, □460.
34 Y. Hey and Y. Zhu, *Chem. Lett*. 2004, **33**, 900.□
35 P. Kanhere, J. Zheng and Z. Chen, *Int. J. Hydrogen Energy* 2012, 37, 4889.□
36 S. H. Lee, K. Teshima, Y. Mizuno, K. Yubuta, T. Shishido, M. Endo and S. Oishi, *CrystEngComm* 2010, **12**, 2871.
37 D. G. Porob and P. A. Maggard, *J. Solid State Chem*. 2006, **179**, 1727.□
38 J. A. Nelson and M. J. Wagner, *J. Am. Chem. Soc.* 2003, **125**, 332.
39 A. Coehlo, *TOPAS Academic*, V 5; Coehlo Software, Brisbane, Australia, **2012.**
40 R.W. Cheary and A. Coelho, *J. Appl. Cryst.* 1992, **25**, 109.
41 V. B. Nalbandyan, I. N. Belyaev and S. I. Rykalova**,** *Rus. J. Inorg. Chem.* 1984, **29**, 996.
42 L Cademartiri and G. A. Ozin. Concepts of Nanochemistry, Wiley-VCH, **2009.**
43 D. Koll, I. Andrusenko, E. Mugnaioli, M. Panthöfer, U. Kolb, W. Tremel, *Z. Anorg. Allg. Chem.* 2013, **639**, 2521.
44 A. Birkel, N. Loges, E. Mugnaioli, M. Panthöfer, U. Kolb, W. Tremel, *Langmuir* 2010, **26**, 3590.